Origin of the Structural Phase Transitions and the Anomalous Electrical and Magnetic Properties of the Magnetic Metal NaV_6O_{11}

Dong-Kyun Seo and Myung-Hwan Whangbo*

Contribution from the Department of Chemistry, North Carolina State University, Raleigh, North Carolina 27695-8204

Received October 19, 1995[⊗]

Abstract: With decreasing temperature, the magnetic metal NaV_6O_{11} undergoes two structural phase transitions (at 245 and 40 K) and exhibits anomalous electrical and magnetic properties. To probe the origin of these structural, electrical, and magnetic properties, the electronic structures of NaV_6O_{11} were calculated for its crystal structures at room temperature, 200 K, and 30 K using the extended Hückel tight-binding band method. The 245 and 40 K structural phase transitions are not caused by a charge density wave instability, but by the lowering of the energy levels lying well below the Fermi level. In the magnetic metallic state of NaV_6O_{11}, obtained by the spin-polarization of the partially filled d-block bands, the electrical conductivity of NaV_6O_{11} is predicted to be greater along the *c*-direction than in the *ab* plane, in agreement with experiment. Our study indicates that the unpaired electrons of NaV_6O_{11} reside mainly in the V_3O_{11} rather than in the V_3O_8 layers. The anomalies of the $\rho_\perp$-vs-*T* plot is explained by considering the effect of disordered magnetic moments on electrical conductivity.

1. Introduction

The electronic structure of a normal metal has one or several partially filled bands, which contain the same number of up-spin and down-spin electrons (Figure 1a). The physical properties of a normal metal are characterized by a decreasing electrical resistivity ρ with decreasing temperature T (Figure 1b) and by a temperature-independent magnetic susceptibility χ (i.e., Pauli paramagnetism) (Figure 1c). The Pauli paramagnetic susceptibility is proportional to the density of states (DOS) at the Fermi level, $n(e_f)$.[1] The magnetic susceptibility of a compound with unpaired electrons obeys the Curie or Curie−Weiss law (i.e., χ^{-1} decreases linearly with decreasing T) in a certain region of temperature (Figure 1d). The intercept with the T axis (i.e., the Weiss temperature θ) in the χ^{-1}-vs-T plot, obtained from the plot in the temperature region above a magnetic (e.g., ferromagnetic or antiferromagnetic) phase transition temperature, is positive for a system with ferromagnetic interactions and negative for a system with antiferromagnetic interactions.[2] A certain metal has unpaired electrons, and its magnetic susceptibility may follow the Curie−Weiss law. From the viewpoint of electronic band structure, one or several partially-filled bands of a magnetic metal are spin-polarized to have unequal numbers of up-spin and down-spin electrons (Figure 1d).[3,4]

Over the years much effort has been devoted to correlate the physical properties of low-dimensional metals with their crystal and electronic structures. Many transition-metal oxide and chalcogenide metals exhibit anomalous electrical and magnetic properties.[5,6] The electronic instability of these compounds leading to their charge density waves (CDW's) is often discussed in terms of Fermi surface nesting.[7−9] The CDW instability driven by Fermi surface nesting refers to the tendency that a low-dimensional metal lowers its electronic energy by opening a band gap at the Fermi level. This is analogous to the first-order Jahn−Teller instability of a molecule, i.e., a molecule with partially filled degenerate HOMO's tends to undergo a symmetry-lowering distortion which splits the degenerate level into the filled and empty ones opening an energy gap between the

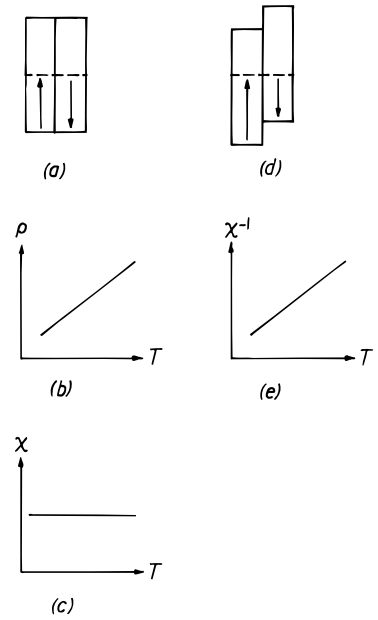

Figure 1. Schematic representations the electronic band structures of normal and magnetic metals and their electrical resistivity (ρ) and magnetic susceptibility (χ) as a function of temperature T: Electronic band structures of normal and magnetic metals are in (a) and (d), respectively, where the dashed lines refer to the Fermi levels. The ρ-vs-T and χ-vs-T relationships of a normal metal are in (b) and (c), respectively. The χ^{-1}-vs-T relationship of a magnetic metal is shown in (e).

[⊗] Abstract published in *Advance ACS Abstracts,* April 15, 1996.

(1) Ashcroft, N. W.; Mermin, N. D. *Solid State Physics*; Saunders College: Philadelphia, 1976.

(2) Kahn, O. *Molecular Magnetism*; VCH: Weinheim, Germany; 1993.

(3) (a) Stoner, E. C. *Proc. R. Soc. London* **1938**, *A165*, 372. (b) Herring, C. In *Magnetism*; Rado, G. T., Suhl, H., Eds.; Academic Press: New York, 1966; Vol. IV.

(4) (a) Hubbard, J. *Phys. Rev. B* **1979**, *19*, 2626. (b) Moriya, T. *J. Magn. Magn. Mater*. **1979**, *14*, 1. (c) Gubanov, V. A.; Liechtenstein, A. I.; Postnikov, A. V. *Magnetism and the Electronic Structure of Crystals*; Springer-Verlag: Berlin, 1992.

0002-7863/96/1518-3951$12.00/0

two.[10] The metal-to-semiconductor phase transition associated with a CDW instability diminishes the $n(e_f)$ value and hence the χ value. A molecule with no partially filled degenerate HOMO's can also undergo a symmetry-lowering distortion, as exemplified by the second-order Jahn−Teller instability.[11] Likewise, the structural modulation of a low-dimensional metal can originate from the lowering of the energy levels lying well below the Fermi level.[9,11]

Sodium hexavanadate NaV_6O_{11} is a magnetic metal with a number of fascinating structural and physical properties.[12−17] Upon cooling from room temperature, NaV_6O_{11} undergoes two structural phase transitions (at 245 and 40 K).[16,17] The magnetic susceptibility of NaV_6O_{11} obeys the Curie−Weiss law above 245 K ($\theta = -81$ K) and between 75 and 110 K ($\theta = 64.2$ K) and exhibits an anomaly at 240 K (Figure 2a).[15] NaV_6O_{11} undergoes a ferromagnetic phase transition at 64 K with the easy axis of magnetization along the crystallographic *c*-direction. The electrical resistivities of NaV_6O_{11} parallel and perpendicular to the *c*-direction ($\rho_{||}$ and $\rho_{\perp}$, respectively) present an interesting temperature-dependence (Figure 2b):[15] $\rho_{||}$ is at least one order of magnitude smaller than $\rho_{\perp}$ at temperatures below room temperature, with $\rho_{||}/\rho_{\perp} = 0.1$ at 300 K. The $\rho_{||}$-vs-*T* plot exhibits a normal metallic character below room temperature, while the $\rho_{\perp}$-vs-*T* plot shows a metallic behavior below 80 K and above 245 K and a weakly semiconducting behavior between 80 and 245 K. In the present work, we probe the origin of the structural phase transitions and apparently complex physical properties of NaV_6O_{11} by calculating the electronic structures of its crystal structures determined by Kanke et al.[16,17] at room temperature, 200 K, and 30 K. For our calculations, the extended Hückel tight-binding (EHTB) method was employed.[19] The parameters of the V and O atoms employed in our EHTB calculations are listed in Table 1.

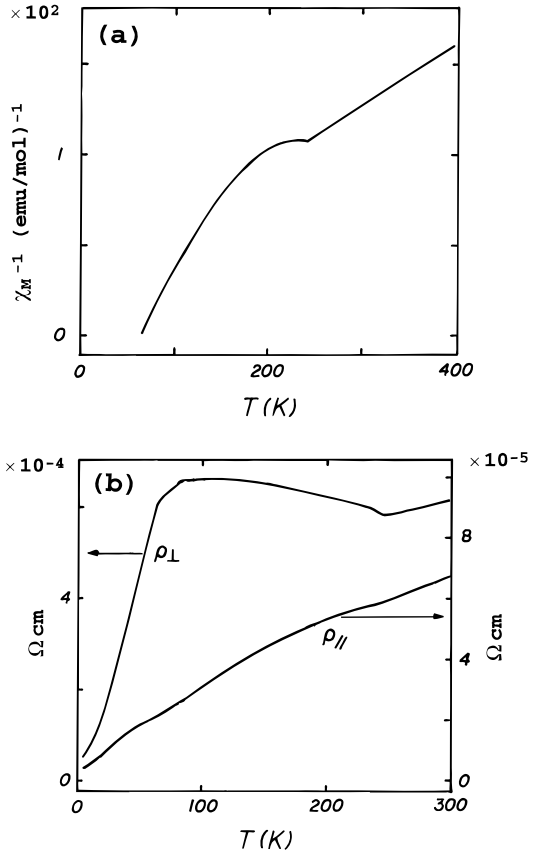

Figure 2. (a) χ^{-1}-vs-*T* and (b) ρ-vs-*T* plots observed for NaV_6O_{11}.

Table 1. Exponents ζ_i and Valence Shell Ionization Potentials H_{ii} of Slater-Type Orbitals χ_i Used for EHTB Calculation[a]

atom	χ_i	H_{ii} (eV)	ζ_i	c_1[b]	ζ_i'	c_2[b]
V	4s	−8.81	1.30			
V	4p	−5.52	1.30			
V	3d	−11.0	4.75	0.4755	1.70	0.7052
O	2s	−32.3	2.275			
O	2p	−14.8	2.275			

[a] H_{ii}'s are the diagonal matrix elements $\langle\chi_i|H^{\text{eff}}|\chi_i\rangle$, where H_{eff} is the effective Hamiltonian. In our calculations of the off-diagonal matrix elements $H^{\text{eff}} = \langle\chi_i|H^{\text{eff}}|\chi_j\rangle$, the weighted formula was used.[24] [b] Contraction coefficients used in the double-ζ Slater-type orbital.

2. Crystal Structure

It is convenient to describe the crystal structure of NaV_6O_{11} in terms of the layers of compositions of V_3O_8 and V_3O_{11}. The V_3O_8 layer of NaV_6O_{11} is made up of edge-sharing VO_6 octahedra (Figure 3 and diagram **1**). At room temperature the

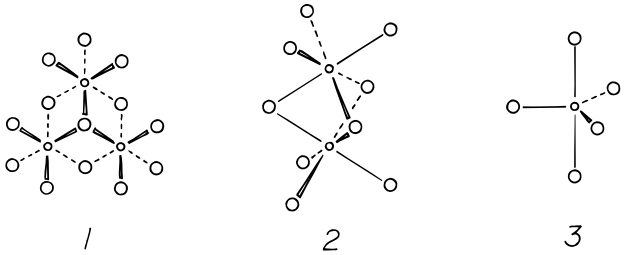

(5) For recent reviews, see: (a) Greenblatt, M. *Int. J. Mod. Phys. B* **1993**, *7*, 3937. (b) Foury, P.; Pouget, J.-P. *Int. J. Mod. Phys. B* **1993**, *7*, 3973. (c) Canadell, E.; Whangbo, M.-H. *Int. J. Mod. Phys. B* **1993**, *7*, 4005. (d) Dumas, J.; Schlenker, C. *Int. J. Mod. Phys. B* **1993**, *7*, 4045. (e) Pouget, J. P. In *Low-Dimensional Electronic Properties of Molybdenum Bronzes and Oxides*; Schlenker, C., Ed.; Kluwer: Dordrecht, The Netherlands, 1989; p 87. (f) Schlenker, C.; Dumas, J.; Escribe-Filippini, C.; Guyot, H. ref 5e, p 159. (g) Greenblatt, M. ref 5e, p 1. (h) Fleming, R. M.; Cava, R. J. ref 5e, p 259. (i) Greenblatt, M. *Chem. Rev.* **1988**, *88*, 31. (j) Schlenker, C.; Dumas, J.; Escribe-Filippini, C.; Guyot, H.; Marcus, J.; Fourcadot, J. *Philos. Mag. B* **1985**, *52*, 643.

(6) For reviews, see: (a) Wilson, J. A.; DiSalvo, F. J.; Mahajan, S. *Adv. Phys.* **1975**, *24*, 117. (b) Williams, P. M. In *Crystallography and Crystal Chemistry of Materials with Layered Structures*; Lévy, F., Ed.; Reidel: Dordrecht, The Netherlands, 1976; Vol. 2, p 51. (c) Monceau, P. In *Electronic Properties of Inorganic Quasi-One-Dimensional Compounds*; Monceau, P., Ed.; Reidel: Dordrecht, The Netherlands, 1985; Part II, p 139. (d) Meerschaut, A.; Rouxel, J. In *Crystal Chemistry and Properties of Materials with Quasi-One-Dimensional Structures*; Rouxel, J., Ed.; Reidel: Dordrecht, The Netherlands, 1986; p 205. (e) DiSalvo, F. J. In *Electron−Phonon Interactions and Phase Transitions*; Riste, T., Ed.; Plenum: New York, 1977; p 107. (f) Friend, H.; Yoffe, A. D. *Adv. Phys.* **1987**, *36*, 1. (g) Withers, R. L.; Wilson, J. A. *J. Phys. C: Solid State Phys.* **1986**, *19*, 4809.

(7) (a) *Structure Phase Transitions in Layered Transition Metal Compounds*; Motizuki, K., Ed.; Reidel: Dordrecht, The Netherlands, 1986. (b) Doni, E.; Girlanda, R. In *Electronic Structure and Electronic Transitions in Layered Materials*; Grasso, V., Ed.; Reidel: Dordrecht, The Netherlands, 1986; p 1.

(8) Canadell, E.; Whangbo, M.-H. *Chem. Rev.* **1991**, *91*, 965.

(9) Whangbo, M.-H.; Canadell, E. *J. Am. Chem. Soc.* **1992**, *114*, 9587.

(10) Albright, T. A.; Burdett, J. K.; Whangbo, M.-H. *Orbital Interactions in Chemistry*; Wiley: New York, 1985.

(11) Whangbo, M.-H.; Seo, D.-K.; Canadell, E. *Physics and chemistry of low-dimensional inorganic conductors*; Schlenker, C., Greenblatt, M., Dumas, J., Van Smaalen, S., Eds.; Plenum: New York, 1996; p 287.

(12) De Roy, M. E.; Besse, J. P.; Chevalier, R.; Gasperin, M. *J. Solid State Chem.* **1987**, *67*, 185.

(13) Kanke, Y.; Takayama-Muromachi, E.; Kato, K.; Matsui, Y. *J. Solid State Chem.* **1990**, *89*, 130.

(14) Kanke, Y.; Izumi, F.; Takayama-Muromachi, E.; Kato, K.; Kamiyama, T.; Asino, H. *J. Solid State Chem.* **1991**, *92*, 261.

(15) Uchida, Y.; Kanke, Y.; Takayama-Muromachi, E.; Kato, K. *J. Phys. Soc. Jpn.* **1991**, *60*, 2530.

(16) Kanke, Y.; Kato, K.; Takayama-Muromachi, E.; Isobe, M. *Acta Crystallogr.* **1992**, *C48*, 1376.

(17) Kanke, Y.; Izumi, F.; Morii, Y.; Akiba, E.; Funahashi, S.; Kato, K.; Isobe, M.; Takayama-Muromachi, E.; Uchida, Y. *J. Solid State Chem.* **1994**, *112*, 429.

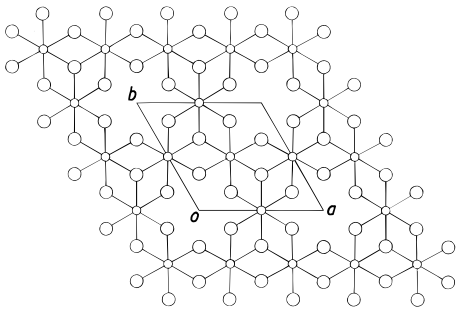

Figure 3. Schematic projection view of the V_3O_8 layer at room temperature along the *c*-direction. The smaller and larger circles represent V and O atoms, respectively.

V atoms of this layer form a Kagomé lattice, so every six V_3 regular triangles share their corners to form a V_6 regular hexagon (Figure 4a). The centers of the V_6 hexagons correspond to those of the "empty O_6 octahedra" of the V_3O_8 layer. Each V_3 triangle has one face and three V−V edges each capped by an oxygen atom (diagram **1**). The face-capping occurs such that the face-capping oxygen atoms form a hexagonal lattice above and below the V-atom plane. At each V atom of the V_3O_8 layer, two edge-sharing octadedral chains intersect. The V_3O_{11} layer of NaV_6O_{11} is composed of face-sharing octahedral dimer V_2O_9 (diagram **2**) and trigonal bipyramid VO_5 (diagram **3**) (Figures 5a and 5b), and each VO_5 unit shares its equatorial oxygen atoms with the middle oxygen atoms of the three neighboring V_2O_9 units. Hereafter, the V atoms of the V_3O_8 layer, the V_2O_9 dimer, and the VO_5 trigonal bipyramid will be referred to as V(1), V(2), and V(3) atoms, respectively.

In NaV_6O_{11} the V_3O_8 and V_3O_{11} layers alternate along the *c*-direction, and adjacent layers are condensed together by sharing their surface oxygen atoms. The axial oxygen atoms of the VO_5 units in the V_3O_{11} layer become the face-capping oxygen atoms of the adjacent V_3O_8 layers. Each empty O_6 octahedron of a V_3O_8 layer is formed from the outside oxygen atoms of the V_2O_9 dimers in the adjacent two V_3O_{11} layers. The Na^+ cations reside at the 12-coordination sites of the V_3O_{11} layers, and each of these sites is made up of three adjacent V_2O_9 dimers.

On lowering the temperature NaV_6O_{11} undergoes two second-order structural phase transitions (at 245 and 40 K).[17] The crystal structure of NaV_6O_{11} at 200 K reveals that the structural transition at 245 K causes a metal-atom trimerization in the V_3O_8 layers such that the Kagomé lattice has two nonequivalent V_3 regular triangles (Table 2 and Figure 4b). In the V_3O_{11} layers, the V−V distance of each V_2O_9 dimer is shortened, and the V atom of each VO_5 trigonal bipyramid moves toward one axial oxygen atom (O_{ax}) (Table 2). As a result of the structural transition at 40 K, the V_3 triangles in the Kagomé lattice of the V_3O_8 layer are converted into isosceles triangles, the V−V distance of each V_2O_9 dimer is further shortened, and the V atom of each VO_5 trigonal bipyramid moves further toward one O_{ax} atom (Table 2 and Figure 4c).

3. Structural Phase Transitions

The Madelung energy calculations for NaV_6O_{11} suggest that the V(1) sites are occupied by V^{3+} (d^2) ions, and the V(2) and V(3) sites by V^{4+} (d^1) ions.[16] To simulate these d-electron counts with electronic structure calculations on isolated layers and molecular fragments, therefore, we employ the $V_3O_8^{7-}$ and $V_3O_{11}^{10-}$ layers and the $V_2O_9^{10-}$ and VO_5^{6-} units. In this section, the relative energies of the $V_6O_{11}^-$ lattices of the room temperature (RT), 200 K, and 30 K crystal structures are estimated by carrying out EHTB electronic band structure calculations for the $V_6O_{11}^-$ lattice and the $V_3O_8^{7-}$ and $V_3O_{11}^{10-}$ layers and also extended Hückel molecular orbital[19] calculations for the $V_2O_9^{10-}$ and VO_5^{6-} units.

Since NaV_6O_{11} is a magnetic metal, the partially-filled d-block bands of the $V_6O_{11}^-$ lattice should be spin-polarized to have unequal numbers of up-spin and down-spin electrons. For our discussion of the relative energies, this spin polarization effect is neglected, i.e., the $V_6O_{11}^-$ lattice and the $V_3O_8^{7-}$ and $V_3O_{11}^{10-}$ layers are assumed to be normal metals. This approximation is not expected to alter the essence of our conclusions, because the extent of the band shifting needed for the spin polarization of NaV_6O_{11} is small (see the next section) and because the stability differences in the RT, 220 K, and 30 K structures arise mainly from those occupied energy levels lying well below the Fermi level (see below). Consequences of the spin polarization on the electrical and magnetic properties of NaV_6O_{11} are discussed in detail in the next section.

Figures 6a and 6b present the contributions of the V(1), V(2), and V(3) atoms to the DOS plots [i.e., projected DOS (PDOS) plots] calculated for the d-block bands of the $V_6O_{11}^-$ lattices at room temperature and 200 K, respectively. Here the dashed line refers to the Fermi level for the normal metallic state of NaV_6O_{11}. The Fermi level occurs within the d-block bands, so NaV_6O_{11} is a metal. Below the Fermi level, the contribution of V(1) to the PDOS is much larger than that of either V(2) or V(3). This is consistent with the conclusion from the Madelung energy calculations that the V(1) sites contain more d-electrons than do the V(2) and V(3) sites.[16] (For further discussion, see the next section.)

The energies of the $V_6O_{11}^-$ lattice, the $V_3O_8^{7-}$ and $V_3O_{11}^{10-}$ layers, and the $V_2O_9^{10-}$ and VO_5^{6-} units for the 200 K and 30 K crystal structures relative to those for the RT crystal structure are summarized in Table 3. The stability of the $V_6O_{11}^-$ lattice is calculated to increase in the order RT < 200 K < 30 K. This trend is consistent with the occurrence of the consecutive 245 and 40 K structural phase transitions on lowering the temperature. Table 3 shows that the 245 K structural phase transition is primarily caused by the stabilization of the $V_3O_8^{7-}$ lattice. The comparison of Figures 6a and 6b reveals that the primary consequence of the structural transition at 245 K is that the bottom portion of the d-block bands associated with the V(1) atoms and lying well below the Fermi level is lowered in energy. In the following, this point is examined in more detail.

The t_{2g}-block bands calculated for the isolated $V_3O_8^{7-}$ layers of the RT and 200 K crystal structures are given in Figures 7a and 7b, respectively. The nine t_{2g}-block bands of the $V_3O_8^{7-}$ layer are divided into three sets with each containing three bands. This can be accounted for by considering the "equatorial planes" of each VO_6 octahedron containing its three t_{2g} orbitals. Each VO_6 octahedron can be represented as in Figure 8a to emphasize the 3-fold symmetry or as in Figures 8b−8d to emphasize the three equatorial planes containing the three t_{2g} orbitals (Figure 8e).[9] As already mentioned, two edge-sharing octahedral chains pass through each V^{3+} ion of the $V_3O_8^{7-}$ layer (Figure 3), and the equatorial planes of these chains are illustrated for a metal trimer unit, V_3O_{13}, in Figures 9a−9d. Two t_{2g} orbitals of each V^{3+} ion are contained in the equatorial planes of these chains (represented with unhatched equatorial planes in Figures 9a−9c),[9] and their σ overlap through the shared octahedral edges leads to the dispersive bands in Figures 7a and 7b (the bottom and top sets). The remaining t_{2g} orbital of each V^{3+} ion, contained in the "isolated" equatorial plane (represented by

(18) Whangbo, M.-H.; Hoffmann, R. *J. Am. Chem. Soc.* **1978**, *100*, 6093.

(19) Hoffmann, R. *J. Chem. Phys.* **1963**, *39*, 1397.

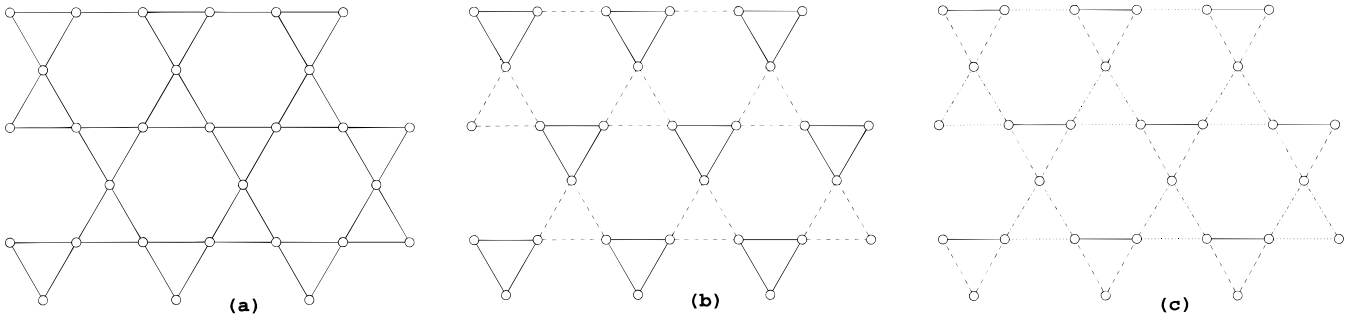

Figure 4. Kagomé lattices of the V atoms in the V_3O_8 layers of the (a) room temperature, (b) 200 K, and (c) 30 K crystal structures of NaV_6O_{11}. V−V = 2.856 Å in the room temperature structure. V−V = 2.746 Å and V- - -V = 2.959 Å in the 200 K structure. V−V = 2.670 Å, V- - -V = 2.779 Å, V-•-V = 2.932 Å, and V···V = 3.011 Å in the 30 K structure.

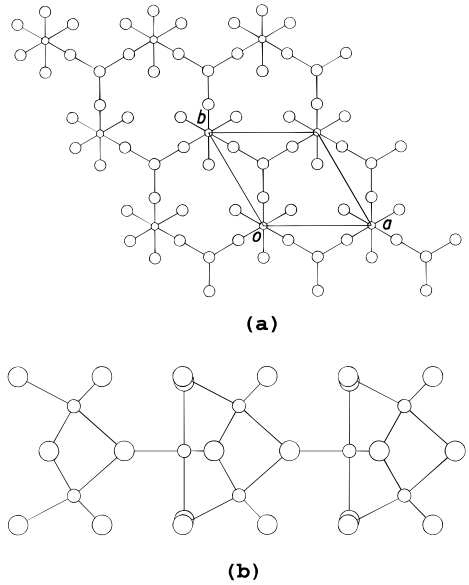

Figure 5. Schematic projection views of the V_3O_{11} layer at room temperature (a) along the *c*-direction and (b) along the *a*-direction. In (a) and (b), the smaller and larger circles represent V and O atoms, respectively.

Table 2. V(1)−V(1), V(2)−V(2), and V(3)−O_{ax} Distances (Å) of the NaV_6O_{11} Crystal Structures Determined at Room Temperature (RT), 200 K, and 30 K

distance	RT	200 K	30 K
V(1)−V(1)	2.856 (×3)	2.746 (×3)	2.670 (×1)
			2.779 (×2)
	2.856 (×3)	2.959 (×3)	2.932 (×2)
			3.011 (×1)
V(2)−V(2)	2.684	2.677	2.665
V(3)−O_{ax}	2.086 (×2)	2.038	1.934
		2.116	2.155

hatching in Figures 9a−9d) with the axial oxygen atoms given by the face-capping oxygen atoms, leads to the nearly flat bands in Figures 7a and 7b (the middle set). For convenience, the t_{2g} orbitals contained in the isolated equatorial planes (Figure 9d) will be referred to as the "tangential" t_{2g} orbitals, and those contained in the edge-sharing octahedral chains as the "radial" t_{2g} orbitals. Then, the bottom and top sets of the bands in Figures 7a and 7b result from the "bonding" and "antibonding" levels between the two "radial" t_{2g} orbitals for each V−V pair of a V_3 triangle, and the middle set from the "nonbonding" levels of each V_3 triangle (i.e., the "tangential" t_{2g} orbitals).

With six d-electrons per unit cell (from three V^{3+} ions), the three "bonding" bands of the $V_3O_8^{7-}$ layer become completely filled thereby leading to a band gap for the RT and 200 K structures (Figures 7a and 7b). For the 200 K structure, the band gap is larger, and the "bonding" bands are lowered in energy, because of the V−V···V bond alternation that takes place along each edge-sharing octahedral chain of the $V_3O_8^{7-}$ layer (Figure 4b). This picture is slightly modified when the $V_3O_8^{7-}$ layers are incorporated into the $V_6O_{11}^{-}$ lattice, because

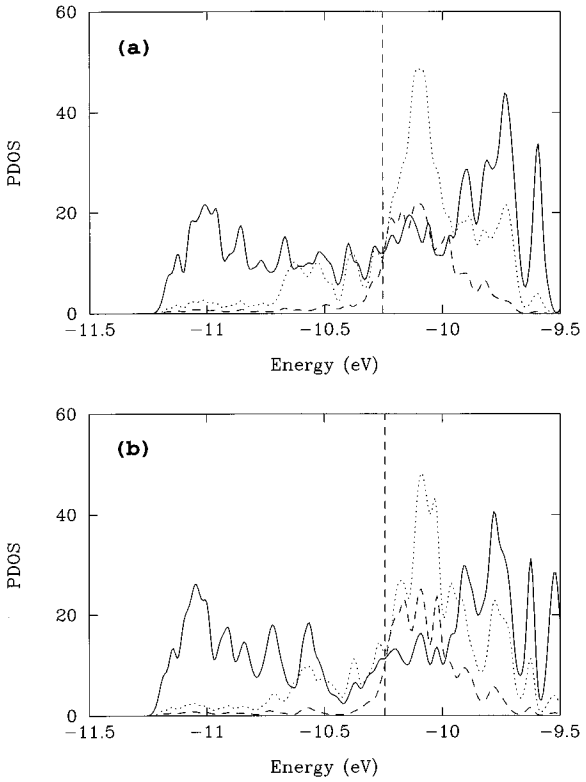

Figure 6. PDOS plots calculated for the $V_6O_{11}^{-}$ lattices of the (a) room temperature and (b) 200 K crystal structures. The dashed lines refer to the Fermi levels of the normal metallic states. The contributions of the V(1), V(2), and V(3) atoms are indicated by the solid, dotted, and dashed lines, respectively.

Table 3. Energies (kcal/mol) of the $V_6O_{11}^{-}$ Lattice, the $V_3O_8^{7-}$ and $V_3O_{11}^{10-}$ Layers, and the $V_2O_9^{10-}$ and VO_5^{6-} Units for the 200 and 30 K Crystal Structures with Respect to the Corresponding Values for the Room Temperature (RT) Crystal Structure[a]

structure	RT	200 K	30 K
$V_6O_{11}^{-}$ lattice	0.0	−8.9	−13
$V_3O_8^{7-}$ layer	0.0	−7.4	−7.1
$V_3O_{11}^{10-}$ layer	0.0	−3.8	−8.4
$V_2O_9^{10-}$ unit	0.0	−3.3	−4.6
VO_5^{6-} unit	0.0	−1.3	−3.8

[a] Energies are per $V_6O_{11}^{-}$, $V_3O_8^{7-}$, $V_3O_{11}^{10-}$, $V_2O_9^{10-}$, and VO_5^{6-} for the $V_6O_{11}^{-}$ lattice, $V_3O_8^{7-}$ and $V_3O_{11}^{10-}$ layers, and $V_2O_9^{10-}$ and VO_5^{6-} units, respectively. The negative energies mean that the 200 and 30 K structures are more stable than the room temperature structure.

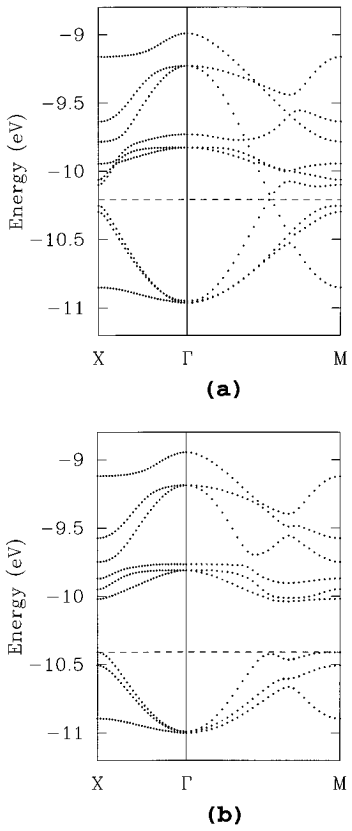

Figure 7. Dispersion relations of the t_{2g}-block bands calculated for the $V_3O_8^{7-}$ layers of the (a) room temperature and (b) 200 K crystal structures, where the dashed lines refer to the highest occupied levels. $\Gamma = (0, 0)$, $X = (a^*/2, 0)$, and $M = (a^*/2, b^*/2)$.

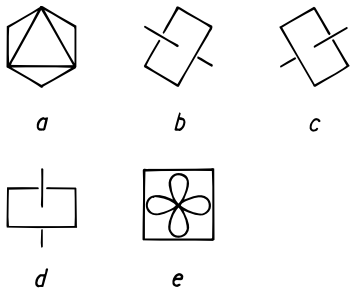

Figure 8. Four different representations of a VO_6 octahedron in (a)−(d). The three t_{2g} orbitals of a VO_6 octahedron are each contained in the equatorial planes of (b)−(d). The t_{2g} orbital contained in an equatorial plane has its orbital lobes pointed to the midpionts of the O_4 square, as illustrated in (e).

their oxygen atoms are shared with those of the $V_3O_{11}^{10-}$ layers. Figures 6a and 6b reveal that the 245 K structural transition does not create a band gap in the PDOS plot of the V(1) atom but substantially reduces its PDOS values in the energy region 0.19 eV below the Fermi level.

Table 3 indicates that the 40 K structural phase transition originates mainly from the stabilization of the $V_3O_{11}^{10-}$ layer. This layer is stabilized because its building blocks, the $V_2O_9^{10-}$ dimers and VO_5^{6-} trigonal bipyramids, are stabilized by the distortions associated with the 40 K phase transition (see Table 2). This stabilization of the $V_3O_{11}^{10-}$ layer is caused by the energy lowering of the oxygen p-block bands lying below the d-block bands and is analogous to a second-order Jahn−Teller distortion. Though not shown, the PDOS plot of the $V_6O_{11}^-$ lattice calculated for the 30 K crystal structure shows that the 40 K structural transition does not open a gap at the Fermi level, as in the case of the 245 K structural transition. Consequently,

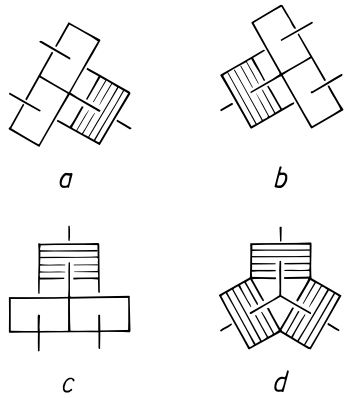

Figure 9. Schematic representation of the equatorial planes containing the t_{2g} orbitals in a trimer unit V_3O_{13} (diagram **1**). As illustrated in (a)−(c), two t_{2g} orbitals of each metal atom are contained in the edge-sharing octahedral chains (represented with unhatched equatorial planes) running throughout the V_3O_8 layer. The remaining t_{2g} orbital of each metal atom is contained in the isolated equatorial plane (represented by hatching). As illustrated in (d), the hatched equatorial planes of a trimer V_3O_{13} unit are "tangential" with respect to the V_3 triangle. The t_{2g} orbitals contained in the unhatched and hatched equatorial planes are referred to as "radical" and "tangential" t_{2g} orbitals, respectively.

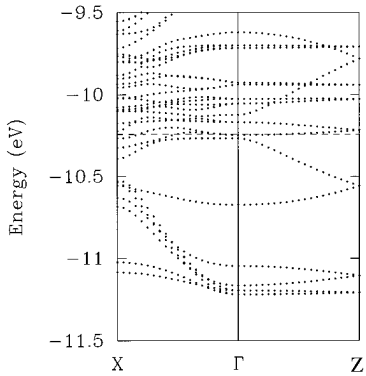

Figure 10. Dispersion relations of the d-block bands calculated for the $V_6O_{11}^-$ lattice of the 200 K crystal structure, where the dashed line refers to the Fermi level of the normal metallic state. $\Gamma = (0, 0, 0)$, $X = (a^*/2, 0, 0)$, and $Z = (0, 0, c^*/2)$.

neither the 245 K nor the 40 K phase transition is of CDW type expected for a system with nested Fermi surfaces.[9,10]

4. Electrical and Magnetic Properties

A. Normal Metallic State. The dispersion relations of the t_{2g}-block bands of the $V_6O_{11}^-$ lattice calculated for the 200 K crystal structure are shown in Figure 10, where the dashed line refers to the Fermi level for the normal metallic state. Hereafter, this Fermi level will be referred to as e_{f0}. The orbital character of these bands can be seen from the PDOS plots given in Figure 6b. In the vicinity of e_{f0}, the PDOS values are smaller below e_{f0} than above e_{f0}, and those above e_{f0} are largely contributed by the V(2) and V(3) atoms.

The Fermi surfaces associated with the normal metallic state (Figures 11a and 11b) are characterized by two spherical Fermi surfaces of nearly equal size centered at Γ and two warped cylinder-like Fermi surfaces running along Γ−Z (i.e., along the *c*-direction). The latter two merge into one in the a^*b^*-plane at the c^*-height of $0.5c^*$. All Fermi surfaces are closed in three directions of the reciprocal space, so NaV_6O_{11} should be a three-dimensional (3D) metal. Due to the cylinder-like Fermi surfaces, however, the direction perpendicular to Γ−Z faces a greater Fermi surface area than does that parallel to Γ−Z. Thus, Figures 11a and 11b predict that the electrical conductivity of

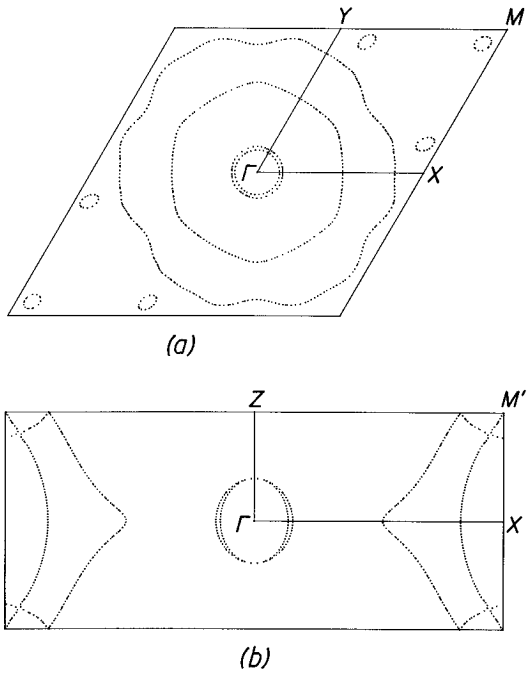

Figure 11. Fermi surfaces of the normal metallic state of the $V_6O_{11}^-$ lattice at 200 K. (a) a^*b^*-plane cross section view at the c^*-height of 0. (b) a^*c^*-plane cross section view at the b^*-height of 0. Y = (0, $b^*/2$, 0), M = ($a^*/2$, $b^*/2$, 0), and M′ = ($a^*/2$, 0, $c^*/2$).

NaV_6O_{11} should be greater along the *c*-direction, in disagreement with the observation that $\rho_{\|}$ is significantly smaller than $\rho_{\perp}$.[15] (Exact details of the Fermi surface shapes depend sensitively on a small change in the Fermi level. However, the essential topological aspects described above remain the same.) To resolve this discrepancy, it is necessary to consider the effects of spin-polarization neglected so far.

B. Spin-Polarized State. The physical properties of a magnetic insulator are determined by strongly localized electrons.[20] In a magnetic metal, which has weakly localized electrons, the local exchange fields associated with them govern the magnetic moment at each atomic site, and the magnetic interactions between the localized moments are mediated by itinerant electrons (i.e., electrons described by electronic band structure).[3,4]

As described in the previous section, the three metal−metal bonding bands of an isolated $V_3O_8^{7-}$ layer are completely occupied by two d-electrons from each V^{3+} ion. In a $V_2O_9^{10-}$ dimer the d-electrons from the two V^{4+} ions can be accommodated in the nondegenerate, metal−metal σ bonding level (Figure 12a). In a VO_5^{6-} trigonal bipyramid, one d-electron from the V^{4+} ion is placed in the doubly-degenerate level (Figure 12b). Thus, one might expect NaV_6O_{11} to have one unpaired electron per formula unit NaV_6O_{11}. However, this argument is approximate, because the building blocks of the $V_6O_{11}^-$ lattice (i.e., the $V_2O_9^{10-}$ and VO_5^{6-} units and the $V_3O_{11}^{10-}$ and $V_3O_8^{7-}$ layers) are fused together by sharing oxygen atoms. The oxygen atom sharing can affect the relative positions of their d-block levels[8] and lead to bands composed of more than one building block. In particular, the LUMO's of $V_2O_9^{10-}$ are doubly-degenerate and lie close to the HOMO of $V_2O_9^{10-}$ and are also close in energy to the HOMO of VO_5^{6-} (Figures 12a and 12b). Thus, the $V_2O_9^{10-}$ units of the $V_3O_{11}^{10-}$ layer may also act as additional sites for unpaired electrons (when the band levels of the $V_6O_{11}^-$ lattice derived largely from the LUMO's of the

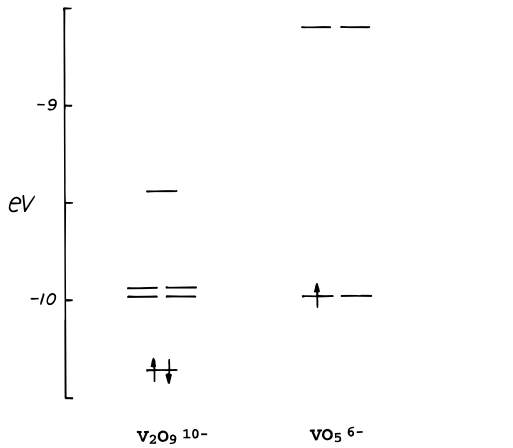

Figure 12. Low-lying d-block energy levels of the $V_2O_9^{10-}$ and VO_5^{6-} units (diagrams **2** and **3**, respectively).

$V_2O_9^{10-}$ units are occupied), thereby increasing the number of unpaired electrons per formula unit in NaV_6O_{11}. Indeed, magnetic susceptibility measurements of NaV_6O_{11} at 5 K show that there are 1.7 unpaired electrons per formula unit.[15]

Within the framework of electronic band structure,[3,4] a magnetic metallic state is obtained from a normal metallic state by introducing spin-polarization. In essence, spin-polarization occurs to reduce the electron−electron repulsion.[21] Suppose a magnetic metal composed of identical sites with on-site repulsion integral U.[20] If the up-spin and down-spin densities at each site are $n\uparrow$ and $n\downarrow$, respectively, the total repulsion per site is given by $n\uparrow n\downarrow U$. This energy term becomes smaller when the $n\uparrow$ and $n\downarrow$ values are different since the total number of electrons at each site is constant ($n\uparrow + n\downarrow$ = constant), i.e., when spin-polarization occurs. In a band picture, spin-polarization can be introduced into a normal metallic state by shifting the up-spin band with respect to the down-spin band (Figure 1d), because this results in unequal numbers of electrons in the two subbands.

In the present work, the spin-polarization in NaV_6O_{11} will be discussed qualitatively by introducing two reasonable assumptions, i.e., that only the partially filled d-block bands are involved in the spin-polarization, and that the essential orbital character of these bands is unaffected by the spin-polarization. With respect to the normal metallic state (Figure 13a), one can obtain more up-spin electrons by raising the Fermi level to $e_{f0} + \Delta\uparrow$, and less down-spin electrons by lowering the Fermi level to $e_{f0} - \Delta\downarrow$ (Figure 13b). When the up-spin and down-spin bands are shifted so that the $e_{f0} + \Delta\uparrow$ and $e_{f0} - \Delta\downarrow$ levels become identical (i.e., adjusted to a new Fermi level e_f), a spin-polarized state results (Figure 13c). Our analysis of the electronic band structure calculated for the 200 K crystal structure of NaV_6O_{11} (Figures 6b and 10) reveals that 1.7 unpaired electrons per formula unit of NaV_6O_{11} are obtained when the $\Delta\uparrow$ and $\Delta\downarrow$ values are 0.045 and 0.208 eV, respectively. (Since these values are small, the relative stabilities of the $V_6O_{11}^-$ lattices at RT, 200 K, and 30 K can be estimated in terms of their normal metallic states, as presented in the previous section.) The $\Delta\uparrow$ value is much smaller than the $\Delta\downarrow$ value because, in the vicinity of e_{f0}, the DOS values are much greater above e_{f0} than below e_{f0}. Note that the V(2) and V(3) atoms have large DOS values in the energy region of $e_{f0} + \Delta\uparrow$. This is so because narrow d-block bands associated with the $V_2O_9^{10-}$ and VO_5^{6-} units of the $V_3O_{11}^{10-}$ layer occur in that energy region (Figures 6b and 10).

C. Electrical Resistivity in the Spin-Polarized State. In Figure 10, the band cut by the Fermi level e_{f0} is narrow along

(20) (a) Mott, N. F. *Metal-Insulator Transitions*; Barnes and Noble: New York, 1977. (b) Brandow, B. H. *Adv. Phys.* **1977**, *26*, 651. (c) Whangbo, M.-H. *J. Chem. Phys.* **1979**, *70*, 4963.

(21) (a) Whangbo, M.-H. *J. Chem. Phys.* **1980**, *73*, 3854. (b) Whangbo, M.-H. *Inorg. Chem.* **1980**, *19*, 1728.

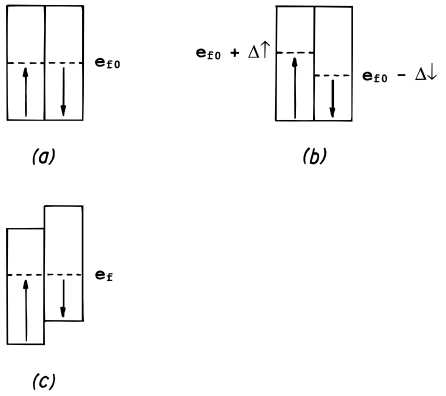

Figure 13. Schematic representation of how the up-spin and down-spin bands of a normal metallic state are spin-polarized to produce a magnetic metallic state within a rigid band scheme: (a) band representation of a normal metallic state, where the numbers of up-spin and down-spin electrons are the same; (b) raising the Fermi level of the up-spin band and lowering that of the down-spin band to produce more up-spin electrons; (c) shifting the up-spin and down-spin bands of (b) to make their Fermi levels identical thereby forming a magnetic metallic state.

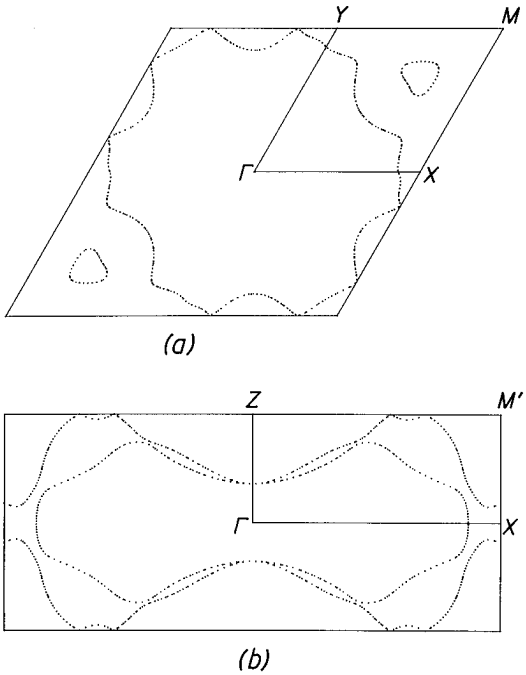

Figure 14. Fermi surfaces associated with the level $e_{f0} + \Delta\uparrow$ of the $V_6O_{11}^-$ lattice at 200 K: (a) a^*b^*-plane cross section view at the c^*-height of 0; (b) a^*c^*-plane cross section view at the b^*-height of 0.

the Γ−Z direction (i.e., *c*-direction). All three metal atoms, V(1), V(2), and V(3), contribute to this band, with the largest contribution from V(3). This band is still cut by the level $e_{f0} + \Delta\uparrow$, since the $\Delta\uparrow$ is small. Immediately below this band, there occurs a band dispersive mainly along Γ−Z, which is cut by the level $e_{f0} - \Delta\downarrow$. This one-dimensional (1D) band (hereafter referred to as the "down-spin 1D band") has almost equal contributions from the V(1) and V(2) atoms. The major contributors of the down-spin 1D band are the tangential t_{2g} orbital of each V(1) atom in the V_3O_8 layer (Figure 9d) and the HOMO (i.e., the σ bonding level) of each $V_2O_9^{10-}$ unit in the V_3O_{11} layer (Figure 12).

The Fermi surfaces associated with the level $e_{f0} + \Delta\uparrow$ (Figure 14) are 3D in nature and suggest a nearly isotropic electrical conductivity for NaV_6O_{11}, since the directions parallel and perpendicular to the *c*-direction face nearly the same Fermi surface area. In contrast, the Fermi surface associated with the down-spin 1D band (Figures 15) predicts a preferential electrical conductivity along the *c*-direction. Consequently, the spin-polarized state of NaV_6O_{11} is predicted to have a greater electrical conductivity along the *c*-direction, in agreement with experiment.

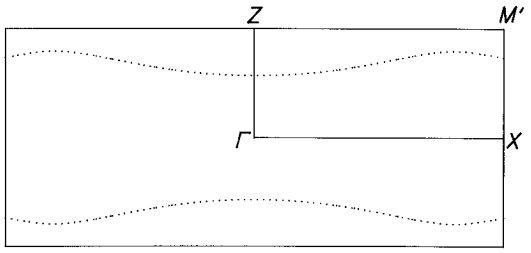

Figure 15. a^*c^*-plane cross section view (at the b^*-height of 0) of the Fermi surface associated with the level $e_{f0} - \Delta\downarrow$ of the $V_6O_{11}^-$ lattice at 200 K.

D. Anomaly in $\rho_\perp$. The $\rho_\perp$-vs-*T* plot of Figure 2b shows an anomaly at 245 K. At this temperature, a metal-atom clustering takes place in the V_3O_8 layer, and a sudden change occurs in the magnetic susceptibility (Figure 2a). The sharp drop of $\rho_\perp$ with decreasing temperature begins at 64 K, and the magnetic moments become ferromagnetically ordered along the *c*-direction at the same temperature. It is of interest to consider a plausible reason for the weakly semiconducting behavior of the $\rho_\perp$-vs-*T* plot (between 80 and 245 K). It is known that disordered magnetic moments can act as scattering centers for conduction electrons and hence cause a semiconducting behavior.[22] Thus, one might speculate that the semiconducting behavior of the $\rho_\perp$-vs-*T* plot arises because the unpaired spins residing in the V_3O_{11} layer are disordered. The absence of a similar behavior in the $\rho_\parallel$-vs-*T* plot (Figure 2b) may arise from the fact that the electrical conductivity is much stronger along the *c*-direction and hence is not so much affected by the spin disorder as is that in the *ab*-plane.

A similar reasoning can account for why the $\rho_\perp$-vs-*T* plot shows a metallic behavior above 245 K. The slope of the χ^{-1}-vs-*T* plot above 245 K is smaller than that below 245 K (Figure 2a). Thus, the effective magnetic moment, $\mu_{eff} \propto [\chi(T - \theta)]^{-1/2}$, is smaller above 245 K, so the electrical conductivity is less affected by disordered magnetic moments above 245 K. Furthermore, due to the metal-atom clustering in the V_3O_8 layer that occurs below 245 K, the $n(e_f)$ value associated with the V(1) atoms of this layer is larger above 245 K than below 245 K. (As noted earlier, Figures 6a and 6b show that the 245 K structural transition reduces the PDOS values of the V(1) atom in the energy region 0.19 eV below e_{f0}. It is in this energy region where the level $e_{f0} - \Delta\downarrow$ occurs.) Above 245 K, therefore, the carrier density in the V_3O_8 layer is higher, and so is the electrical conductivity in the *ab*-plane. This factor also makes the electrical conductivity less susceptible to the scattering effect of disordered magnetic moments.

E. Magnetic Ordering in the Spin-Polarized State. Our electronic structure study indicates that unpaired electrons of NaV_6O_{11} reside largely in the V_3O_{11} rather than in the V_3O_8 layers. Thus, the occurrence of a ferromagnetic ordering in NaV_6O_{11} below 64 K, with the easy axis of magnetization along the *c*-direction, implies that the unpaired electrons of the V_3O_{11} layers couple ferromagnetically through the V_3O_8 layer. In terms of the spin-polarization mechanism of ferromagnetic

(22) (a) Searle, C. W.; Wang, S. T. *Can. J. Phys.* **1970**, *48*, 2023. (b) Cox, P. A. *Transition Metal Oxides*; Oxford University Press: New York, 1992.

coupling,[23] one might suggest that the V_3O_8 layers act as a spin-polarization medium. The down-spin 1D band of NaV_6O_{11} (Figure 10), which have orbital contributions almost equally from the V_3O_8 and the V_3O_{11} layers, may provide low-lying excited states needed for the configuration interactions leading to the ferromagnetism.

If the V_3O_8 layer acts as a spin-polarizing medium, any structural change in the layer should affect the magnetic susceptibility. Indeed, the χ^{-1}-vs-T plot exhibits an anomaly at around 245 K (Figure 2a), where the metal-atom trimerization takes place in the V_3O_8 layer. Figure 2a shows that the linear part of the χ^{-1}-vs-T plot predicts ferromagnetic interactions below 245 K ($\theta = 64.2$ K) and antiferromagnetic interactions above 245 K ($\theta = -81$ K). Therefore, the V_3O_8 layer without metal trimerization (above 245 K) acts as a medium for antiferromagnetic coupling, while that with metal trimerization (below 245 K) acts as a medium for ferromagnetic coupling.

5. Concluding Remarks

We probed the origin of the structural phase transitions and the unusual electrical and magnetic properties of NaV_6O_{11} by calculating the electronic structures of its structures at RT, 200 K, and 30 K. The 245 K and the 40 K structural phase transitions are not driven by a CDW instability associated with nested Fermi surface, but by the lowering of the energy levels lying well below the Fermi level. The transition at 245 K is caused by the metal-atom clustering in the V_3O_8 layers, and the 40 K transition is caused by the distortions of the V_2O_9 and VO_5 units in the V_3O_{11} layers.

In the normal metallic state the electrical conductivity of NaV_6O_{11} is expected to be nearly isotropic. In the magnetic metallic state of NaV_6O_{11}, obtained by the spin-polarization of the partially filled d-block bands, the electrical conductivity of NaV_6O_{11} is predicted to be greater along the *c*-direction than in the *ab*-plane, in agreement with experiment. Our study indicates that the unpaired electrons of NaV_6O_{11} reside mainly in the V_3O_{11} rather than in the V_3O_8 layers. The anomalies of the $\rho_\perp$-vs-T plot can be explained by taking into consideration the effect of disordered magnetic moments on electrical conductivity. It is interesting that, for the unpaired electrons of the V_3O_{11} layers, the V_3O_8 layers with metal-atom trimerization (below 245 K) act as a ferromagnetic coupling medium, but those without metal-atom trimerization (above 245 K) act as an antiferromagnetic coupling medium.

In the extended Hückel method, the matrix elements of the effective Hamiltonian are determined semiempirically and they are not adjusted self-consistently. In addition, electron−electron interactions are not taken into consideration. Consequently, this method cannot be used to optimize molecular and crystal structures though it is useful in discussing the electronic properties of compounds with known structures. EHTB calculations have been indispensable in describing the electronic structures of numerous organic and inorganic solid-state materials.[8,9,25,26] Even for magnetic insulators, molecular orbitals generated by the extended Hückel method provide a basis for considering magnetic interactions between spin centers.[2,23,27] The present work strongly suggests that the electronic structure of a magnetic metal can also be described on the basis of EHTB calculations.

Acknowledgment. This work was supported by the U.S. Department of Energy, Office of Basic Sciences, Division of Materials Sciences, under Grant No. DE-FG05-86ER45259.

JA953508O

(23) (a) Kollmar, C.; Kahn, O. *J. Am. Chem. Soc.* **1991**, *113*, 7994. (b) Kollmar, C.; Kahn, O. *Acc. Chem. Res.* **1993**, *26*, 259.

(24) Ammeter, J.; Bürgi, H.-B.; Thibeault, J.; Hoffmann, R. *J. Am. Chem. Soc.* **1978**, *100*, 3686.

(25) Williams, J. M.; Ferraro, J. R.; Thorn, R. J.; Carlson, K. D.; Geiser, U.; Wang, H. H.; Kini, A. M.; Whangbo, M.-H. *Organic Superconductors*; Prentice Hall: Englewood Cliffs, 1992, and references cited therein.

(26) Magonov, S. N.; Whangbo, M.-H. *Surface Analysis with STM and AFM*; VCH: Weinheim, 1996.

(27) Hay, P. J.; Thibeault, J. C.; Hoffmann, R. *J. Am. Chem. Soc.* **1975**, *97*, 4884.